Available online at www.sciencedirect.com

ScienceDirect

Underground Space 25 (2025) 1–18

www.keaipublishing.com/undsp

Research Paper

Effects of geothermal temperature on smoke dynamics in construction tunnel fires

Chuangang Fan [a,b], Xiaoxian Fei [a,b], Maozhen Liu [a,b], Jiayi Ha [a,b], Linbo Du [a,b], Zhi Li [c], Yuhao Li [d], Dia Luan [a,b,e,*]

[a] School of Civil Engineering, Central South University, Changsha 410075, China
[b] Hunan Provincial Key Laboratory for Disaster Prevention and Mitigation of Rail Transit Engineering Structures, Central South University, Changsha 410075, China
[c] School of Resources and Safety Engineering, Central South University, Changsha 410000, China
[d] Hunan Provincial Communications Planning, Survey & Design Institute CO., LTD., Changsha 410200, China
[e] Department of Fire Protection Engineering, Southwest Jiaotong University, Chengdu 611756, China

Received 14 July 2024; received in revised form 8 April 2025; accepted 31 May 2025
Available online 16 September 2025

Abstract

The development of traffic networks in mountainous areas has led to an increasing number of tunnels being constructed in regions of high geothermal activity. This study examined the effects of geothermal temperature, heat release rate, and fire source location on temperature distribution and smoke movement in construction tunnel fires through a series of scaled-down experiments. Results showed that geothermal conditions heat the air, creating layered flow within construction tunnels. The temperature and velocity of the induced airflow along the tunnel length were characterized. The upper airflow caused by geothermal conditions hinders the spread of smoke toward the tunnel face, resulting in a complex thermal stratification phenomenon. A model for predicting the smoke diffusion length upstream of the fire source was developed, considering geothermal temperature, heat release rate, and fire source location. Additionally, the ceiling temperature distribution was analyzed, showing that downstream temperature decay is insensitive to fire location, while upstream temperature decay can be divided into geothermal-affected and non-affected zones based on the fire source position. Prediction models for the ceiling temperature distribution upstream and downstream were established, respectively. These findings enhance the understanding of smoke dynamics in construction tunnel fires under high geothermal conditions.

Keywords: Geothermal temperature; Construction tunnel fire; Smoke dynamics; Thermal stratification; Ceiling temperature distribution

1 Introduction

In recent years, the rapid development of transportation networks has led to an increase in the design and construction of tunnels (L. Chen et al., 2023; Wan et al., 2023). Unlike regular tunnels, construction tunnels present unique challenges because the tunnel face remains blocked during construction. In the event of a fire, smoke can only escape through the tunnel entrance, which also serves as the sole evacuation route for personnel. The absence of comprehensive smoke exhaust measures in construction tunnels poses a significant threat to the safe evacuation of workers. As a result, scholars have focused on fire safety during tunnel construction, particularly on smoke movement in construction tunnel fires (Yao et al., 2017; Ye et al., 2021; Liu et al., 2023).

As tunnel construction advances in length, depth, and scale (Guo et al., 2021; X. Chen et al., 2023; Liu et al., 2025), high geothermal environments have become increasingly prevalent in tunnel projects (Zhang et al., 2022; Wang

* Corresponding author at: School of Civil Engineering, Central South University, Changsha 410075, China.
E-mail address: luandie@swjtu.edu.cn (D. Luan).
Peer review under the responsibility of Tongji University

https://doi.org/10.1016/j.undsp.2025.05.004

Nomenclature

a, b, c	Fitting coefficient in Eq. (6)
c_p	Air specific heat capacity (kJ/(kg·K))
D_f	Fire source location (m)
g	Gravitational acceleration (m/s^2)
H	Tunnel height (m)
H	Hydraulic tunnel height (m)
ΔH_c	Total heat of combustion (MJ/kg)
L	Smoke diffusion length (m)
$\dot{m}$	Mass burning rate (kg/s)
Q	Heat release rate (kW)
r	Distance between temperature measuring point and reference point (m)
t	Time (s)
T	Temperature (K)
T_g	Geothermal temperature (K)
ΔT	Temperature rise (K)
ΔT_g	Ceiling temperature rise induced by geothermal condition (K)
$\Delta T_{g,\Delta x}$	Ceiling temperature rise at a distance Δx from boundary between geothermal zone and non-geothermal zone (K)
ΔT_r	Temperature rise at a distance r from reference point (K)
V	Velocity (m/s)
V_g	Airflow velocity below the tunnel ceiling induced by geothermal condition (m/s)
x	Distance from the tunnel face (m)
Δx	Distance from the boundary between geothermal zone and non-geothermal zone (m)

Superscript/subscript

F	Full-scale tunnel
M	Reduced-scale tunnel
g	Geothermal condition
max	Maximum
*	Dimensionless
0	Ambient

Greek symbols

γ	Reduced scale
μ, φ	Fitting coefficient in Eq. (8)
ρ	Air density (kg/m^3)
χ	Combustion efficiency

et al., 2023). For example, the Sichuan-Xizang Railway in China, currently under construction, is located on the Qinghai-Xizang Plateau, within one of the world's five high-temperature geothermal zones known as the Tethys (Mediterranean-Himalayan) convergent plate boundary geothermal belt (Zhang et al., 2017). With the increasing number of tunnels being built in high geothermal regions in recent years (Liu et al., 2024), these geological conditions pose significant threats to electronic and mechanical systems. Such environments can cause short circuits and equipment damage, potentially leading to tunnel fires (K. Zhao et al., 2023). Additionally, the high geothermal environment causes severe discomfort to construction workers (Hu et al., 2019), resulting in symptoms such as confusion, fatigue, and slowed reactions (Yu, 2015), which significantly increases the likelihood of operational errors and subsequent fires. Therefore, it is crucial to conduct studies on tunnel fires in high geothermal environments during construction.

The distribution of smoke temperature below the tunnel ceiling has been extensively studied for its role in indicating structural damage and smoke diffusion (Tao & Bobet, 2016; Han et al., 2022; J. Zhao et al., 2023a). Ye et al. (2019) conducted full-scale experiments in a construction tunnel to develop a predictive model for ceiling temperature decay. Gao et al. (2021) conducted numerical simulations to investigate the temperature distribution in a tunnel with one end blocked. Results showed that the maximum ceiling temperature rise can be categorized into two zones based on the distance between the fire source and the blocked end. When the ratio of the distance from the fire source to the tunnel height (D_f/H) is less than 1, the maximum temperature rise increases as the fire source approaches the blocked end. However, when D_f/H is greater than 1, the blocked end does not affect the maximum temperature rise. G. Xu et al. (2021) studied the linear fire source in a sealed tunnel and proposed a bi-exponential model for predicting ceiling temperature distribution. Li et al. (2023) performed a series of experiments in a scaled model tunnel with one end blocked and established a predictive formula for ceiling temperature distribution, considering the tunnel's slope and heat release rate. Gao et al. (2024) found that the presence of a blocked end slows ceiling temperature decay through numerical simulation. Tang et al. (2024) utilized numerical simulations to study the impact of tunnel aspect ratio on smoke movement in construction tunnels. Results indicated that construction tunnels exhibit a significantly higher maximum ceiling temperature rise than regular tunnels, with a greater aspect ratio leading to a more substantial increase. Luan et al. (2025) investigated the effect of rainfall on fire development and smoke dynamics in a tunnel with one end blocked, observing the destruction of the smoke layer.

However, the effect of geothermal conditions on smoke dynamics in construction tunnel fires remains unknown. In construction tunnels exposed to geothermal conditions, the higher temperature near the tunnel face results in an uneven temperature distribution along the tunnel. Xu

et al. (2022) found that the buoyant flow generated by convective heat transfer in geothermal tunnels significantly affects both the temperature and airflow within the tunnel, and a three-dimensional dynamic heat transfer model for high geothermal tunnels has been established. Yang et al. (2023) found that the air in geothermal tunnels is heated by high-temperature rocks, creating buoyant flows in which hot air rises and cold air sinks, leading to layered flow patterns. D. Xu et al. (2023) conducted a numerical investigation of the temperature field in a tunnel under geothermal conditions and observed that the temperature along the tunnel exhibited an "N" shape.

It is foreseen that the influence of the coupled effects of the blocked tunnel face and geothermal conditions on the temperature and flow fields in construction tunnels will be exacerbated. In such scenarios, the movement of smoke and the temperature distribution are expected to be asymmetric and complex. This work aims to investigate the characteristics of smoke movement and ceiling temperature distribution in construction tunnel fires under geothermal conditions through a series of scaled-down experiments. The findings can provide a theoretical basis for fire detection, smoke control, evacuation, and rescue design in construction tunnel fires under geothermal conditions.

2 Experiment setup

This study employs the Froude similarity criterion, which has been widely validated in fire research (Chaabat et al., 2019; Ouyang et al., 2021; Fan et al., 2023). A 1:20 scale model tunnel was constructed, and the similarity relationships of the key experimental parameters are shown in Table 1.

The vault model tunnel, depicted in Fig. 1(a), measures 10 m in length and 0.6 m in width, with a maximum height of 0.63 m and a rectangular section height of 0.43 m. It is divided into a 3-m geothermal zone and a 7-m non-geothermal zone, corresponding to 60 m and 140 m in full scale, respectively. The arched top of the non-geothermal zone is made of 2-mm-thick galvanized steel plates, while the tunnel floor and one side wall are constructed of fireproof boards. The other side wall is composed of 10-mm-thick fireproof glass to allow observation of flame and smoke behavior. The geothermal zone is constructed from 30-mm-thick concrete plates supported by a 3-mm-thick steel frame. During the experiments, the front concrete cover will be replaced with a 1-m-long, 10-mm-thick fireproof glass panel at the fire source position.

Table 1
Similarity relationships of key parameters.

Parameter	Relational expression	
Heat release rate (kW)	$Q_M = Q_F\gamma^{5/2}$	(1)
Velocity (m/s)	$V_M = V_F\gamma^{1/2}$	(2)
Temperature (K)	$T_M = T_F$	(3)
Time (s)	$t_M = t_F\gamma^{1/2}$	(4)

In geothermal tunnels, supports, linings, and insulation materials are typically applied after excavation to mitigate the effects of geothermal conditions on the tunnel environment (Zhao et al., 2021). Hu et al. (2021) found that the temperature of the supports drops rapidly within 5–7 days, while Wang et al. (2020) observed that the temperature drop during the first 5 days accounts for 92.7%–94.8% of the total temperature reduction. Additionally, excavation rates in tunnels affected by geothermal conditions generally do not exceed 10 m per day (Armaghani et al., 2019; Z. Xu et al., 2021). Therefore, a full-scale geothermal section of 60 m in length was selected as the focus of this study, with a corresponding reduced scale of 3 m for the model tunnel.

2.1 Geothermal condition simulation

A geothermal heating device, consisting of flexible heating panels, temperature measurement points, and a temperature controller with a range of 0–150 °C and an accuracy of ±2 °C , was used to simulate geothermal conditions. The flexible heating panels were installed on the outer surface of the concrete wall in the geothermal section to heat the concrete and simulate the geothermal environment. The temperature measured on the inner surface of the tunnel was used as the geothermal temperature during the experiments.

Ten K-type patch thermocouples were distributed on the inner top surface and both inner sides of the geothermal zone of the tunnel for real-time temperature monitoring. Specifically, six thermocouples were arranged along the centerline of the tunnel ceiling and rear side panels at distances of 0.5, 1.5, and 2.5 m from the tunnel face. The remaining four thermocouples were arranged along the centerline of the tunnel floor and front side panels at the same intervals, with their locations adjusted to avoid the fire source region. For example, if the fire source was at 1.5 m, the thermocouples on the front side and floor were arranged at 0.5 and 2.5 m, respectively. Figure 2(a) shows the average temperature of the ten thermocouples over time, indicating that the temperature of the tunnel's inner wall in the geothermal zone was maintained near the desired value, with an error margin within 5%. The ignition experiment was started after 300 s of monitoring a stable temperature, ensuring that a stable temperature field and flow field had been established in the tunnel before fuel ignition.

2.2 Fire source and measuring setting

Anhydrous ethanol was chosen as the fuel. Square fire pans of three different sizes of 64, 100, and 144 cm^2 were used as containers to investigate the effects of varying heat release rates (HRRs). The corresponding HRRs under full-scale tunnel fire conditions, without considering geothermal effects, were 4.3, 7.2, and 11.0 MW for the three fuel pool sizes, respectively. The initial fuel thickness was maintained at 1 cm to ensure a stable combustion phase. An

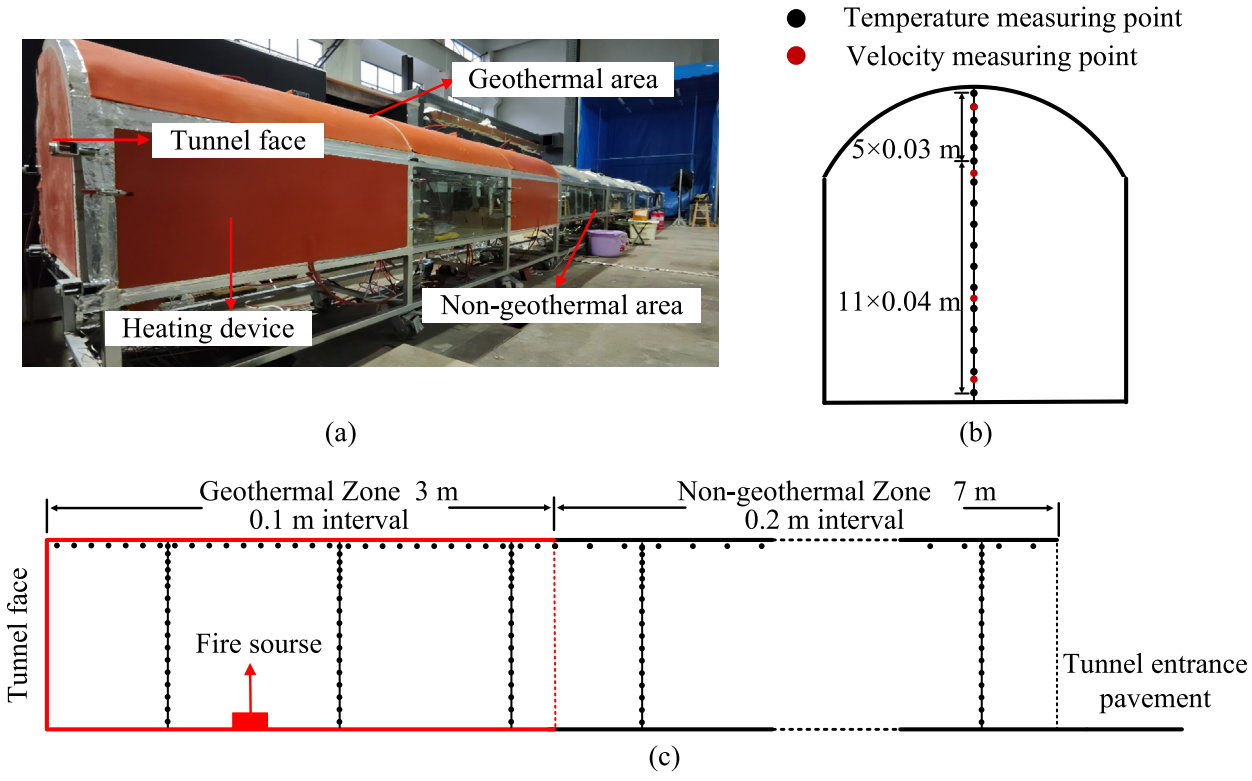

Fig. 1. Experiment setup of the model tunnel. (a) Photograph of the tunnel model, (b) side view, and (c) front view.

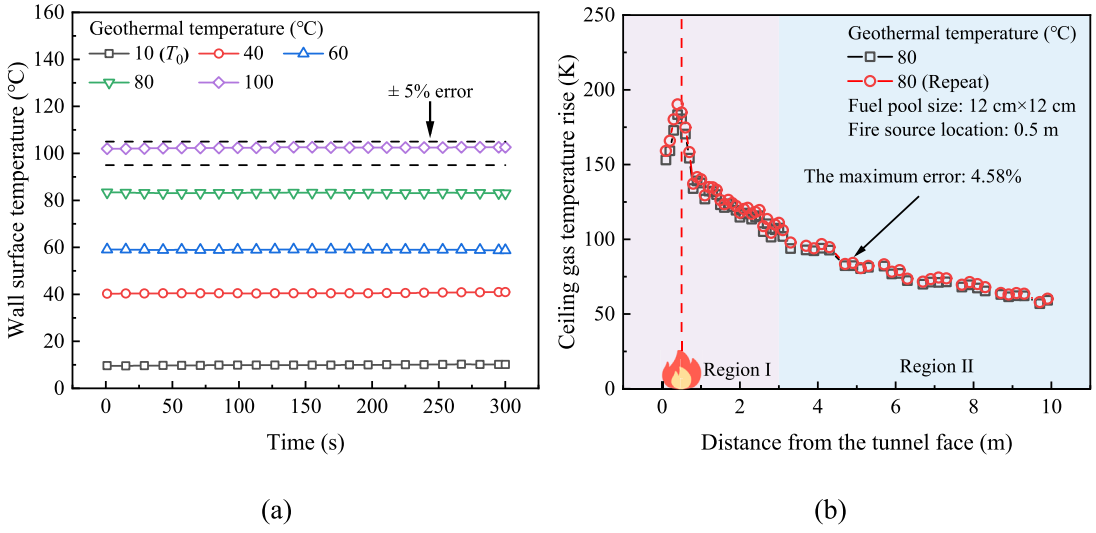

Fig. 2. Geothermal temperature monitoring and reproducibility verification of tests. (a) Geothermal temperature monitoring before fuel ignition, and (b) reproducibility verification of experimental tests.

electronic balance (type: XS-30001 TS, maximum capacity: 30 kg, accuracy: 0.1 g, sampling frequency: 1 s) was used to measure the fuel mass loss during the experiments. The HRR of the fire was calculated using the following equation:

$$Q = \chi \times \dot{m} \times \Delta H_c. \quad (5)$$

Here, the combustion efficiency χ and the heat of complete combustion ΔH_c are 1 and 26.8 kJ/g for liquid anhydrous ethanol, respectively. K-type thermocouples (1 mm in diameter) were used to measure the temperature field. Ceiling thermocouples were positioned along the longitudinal centerline of the tunnel, 20 mm below the ceiling. Thermocouples were spaced 0.1 m apart in the geothermal zone and 0.2 m apart in the non-geothermal zone. Additionally, 10 sets of thermocouple trees were arranged at distances of 0.75, 1.75, 2.75, 3.5, 4.5, 5.5, 6.5, 7.5, 8.5, and 9.5 m from the tunnel face to measure the vertical temperature

distribution, as shown in Fig. 1(b) and (c). It is important to note that the thermocouple trees were not placed directly above the fire source to avoid interference with the flame geometry characteristics. During the experiment, a four-probe anemometer (type: KANOMAX-KA12, maximum capacity: 0–5 m/s, accuracy: 0.1 m/s, sampling frequency: 0.1 s) was used to measure the airflow velocity in the tunnel. The four probes were positioned 5 cm and 20 cm from the top and bottom of the tunnel, respectively (see Fig. 1). Measurements were taken at eleven cross-sections positioned 0.5, 1.5, 2.5, 3, 4, 5, 6, 7, 8, 9, and 10 m away from the tunnel face. At each cross-section, wind speeds were recorded for 5 min to ensure data stability. These data were used to construct a plot of the overall flow field within the tunnel.

2.3 Test condition and repeatability verification

Five geothermal temperatures (10, 40, 60, 80, and 100 °C), seven fire source locations (0.5, 1.5, 2.5, 4, 6, 8, and 10 m away from the tunnel face), and three fuel pool sizes (8 cm × 8 cm, 10 cm × 10 cm, and 12 cm × 12 cm) were considered in this study. A total of 105 tests were conducted, with the specific parameters listed in Table 2.

Conditions 1–21 were designated as control groups, with the heating device turned off to compare the effects of geothermal conditions. Throughout the experiments, the ambient temperature remained relatively stable at around 10 °C , which was consistently used as the ambient temperature. Each experimental set was repeated at least twice to ensure reliability. Figure 2(b) shows the reproducibility verification for a case with a fuel pool size of 12 cm × 12 cm, a fire position 0.5 m away from the tunnel face, and a geothermal temperature of 80 °C . A maximum temperature rise error of less than 5% indicates the reliability of the experiments.

3 Results and discussion

3.1 Temperature field and flow field without fire

Figure 3(a) illustrates the development of layered flows in geothermal tunnels during construction. High-temperature rocks heat the air in the geothermal zone, generating thermal plumes that rise and accumulate beneath the tunnel ceiling. Due to the presence of tunnel face, the hot air is confined and spreads along the tunnel ceiling toward the open end. As the hot air exits the tunnel, cold external air enters from the tunnel bottom to maintain mass balance, creating opposing layered flows. This phenomenon has also been reported by Yang et al. (2023). Subsequently, the incoming cold air in the geothermal zone undergoes heat exchange with the hot air, reducing the dominance of thermal plumes in the airflow direction. As a result, a complete non-isothermal flow cycle forms, moving from the tunnel floor along the blocked wall and then along the ceiling toward the open end, as shown in Fig. 3 (b).

Figure 4 shows the temperature and velocity contours within the geothermal tunnel, exhibiting a pronounced vertical stratification pattern. Notably, temperature data at the 10-m position and airflow speed data at the 0-m position were unobtainable due to limitations in measurement placement. The highest temperature and maximum wind velocity were recorded at the boundary between the geothermal and non-geothermal sections. This phenomenon can be attributed to the continuous heating of hot air beneath the tunnel ceiling in the geothermal zone, which leads to enhanced thermal buoyancy and velocity. As the hot air exits the geothermal zone, it undergoes heat exchange with the cooler tunnel walls and lower air, causing a decrease in temperature and a subsequent reduction in buoyancy and velocity.

Figure 5 shows the temperature and velocity distribution along the tunnel ceiling under varying geothermal temperatures, as reported in our previous study (Fei et al., 2025). Velocity data were collected 5 cm below the tunnel ceiling. It is observed that the patterns of temperature and velocity distribution along the tunnel ceiling appear consistent across different geothermal temperatures. The ceiling temperature remains consistent in the geothermal zone but decreases in the non-geothermal zone. In the geothermal zone, the velocity increases with distance from the tunnel face and stabilizes along the length of the tunnel in the non-geothermal zone. Both temperature and velocity show a noticeable drop at the boundary between the geothermal and non-geothermal zones.

The temperature difference ΔT_g between the geothermal temperature T_g and the ambient temperature T_0 is set as a reference, and the temperature along the tunnel ceiling is analyzed. The ceiling temperature distribution in the non-geothermal zone follows a bi-exponential model; hence,

Table 2
Experimental conditions.

No.	Geothermal temperature (°C)	Fire source location (m)	Fuel pool size
1–21	Ambient temperature (10)	0.5, 1.5, 2.5, 4, 6, 8, 10	8 cm × 8 cm
22–42	40		10 cm × 10 cm
43–64	60		12 cm × 12 cm
65–85	80		
86–105	100		

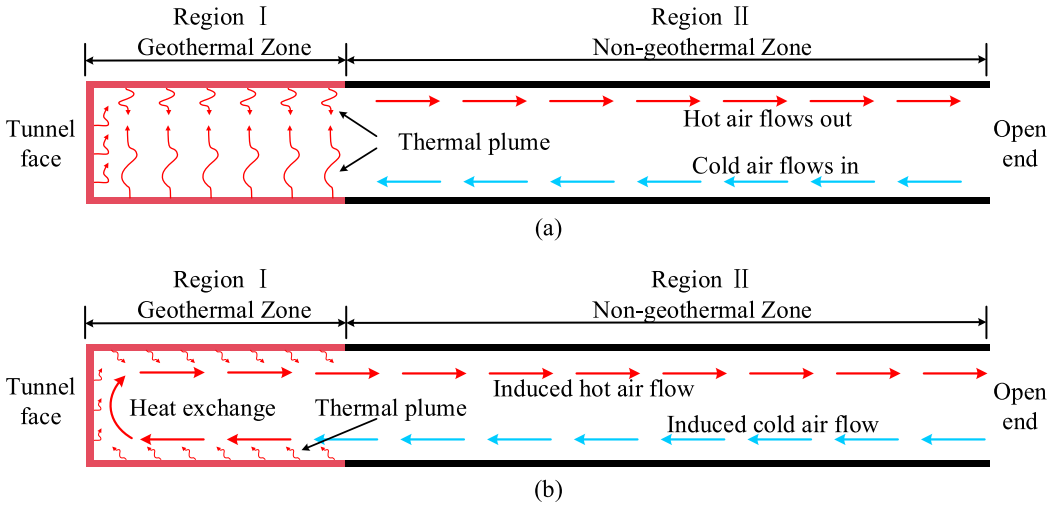

Fig. 3. Flow field in geothermal tunnels during construction. (a) Layered flow formation stage, and (b) layered flow stable stage.

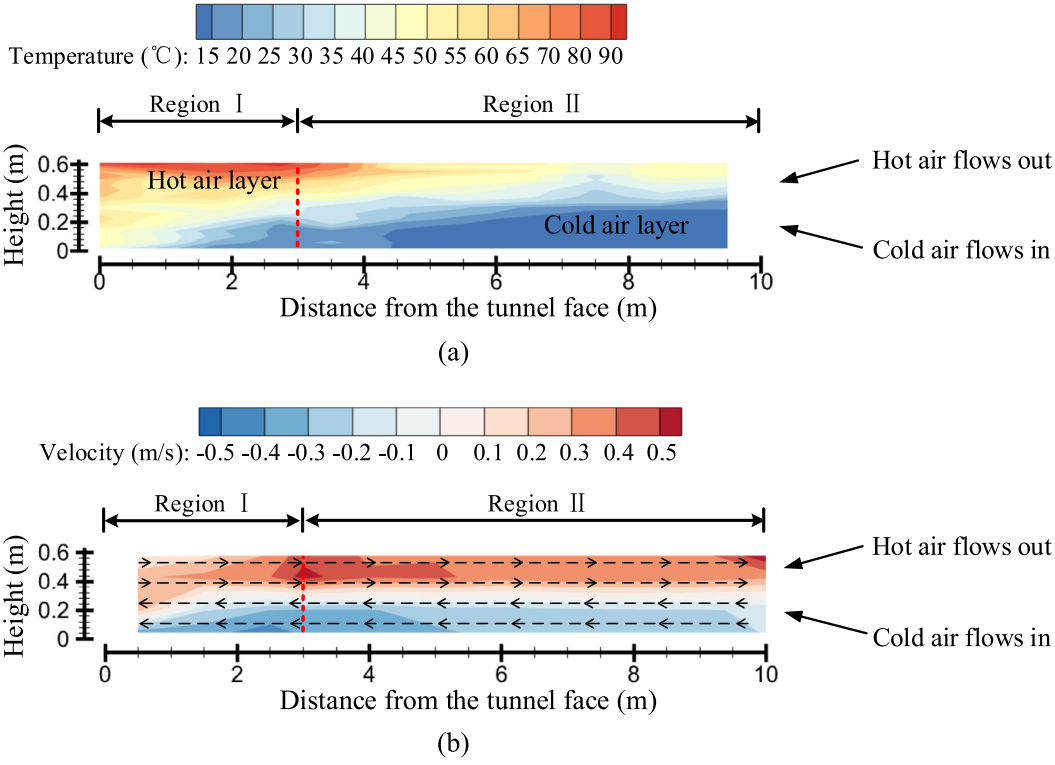

Fig. 4. Temperature and velocity contours within the geothermal tunnel (T_g = 100 °C). (a) Temperature contour, and (b) velocity contour.

the temperature along the tunnel ceiling can be expressed as follows:

$$\frac{\Delta T_{g,\Delta x}}{\Delta T_g}=\begin{cases}1, & \text{region I}\\ a\exp\left(-b\frac{\Delta x}{H}\right)+(1-a)\exp\left(-c\frac{\Delta x}{H}\right), & \text{region II}\end{cases}. \tag{6}$$

Figure 6 shows the temperature distribution along the tunnel ceiling in the non-geothermal zone. As a result, the ceiling temperature distribution in a construction tunnel under geothermal conditions can be predicted by Eq. (7).

$$\frac{\Delta T_{g,\Delta x}}{\Delta T_g}=\begin{cases}1, & \text{region I}\\ 0.67\exp\left(-0.06\frac{\Delta x}{H}\right)+0.33\exp\left(-2.50\frac{\Delta x}{H}\right), & \text{region II}\end{cases}. \tag{7}$$

The dimensionless airflow velocity and dimensionless geothermal temperature are introduced as $V_g^*=V_g/\sqrt{g\bar{H}}$ and $T_g^*=T_g/T_0$, respectively. Consequently, in the geothermal zone, the airflow velocity increases approximately linearly with distance from the tunnel face, and the increase rate depends on the geothermal temperature, as shown in Fig. 7(a). In the non-geothermal zone, the

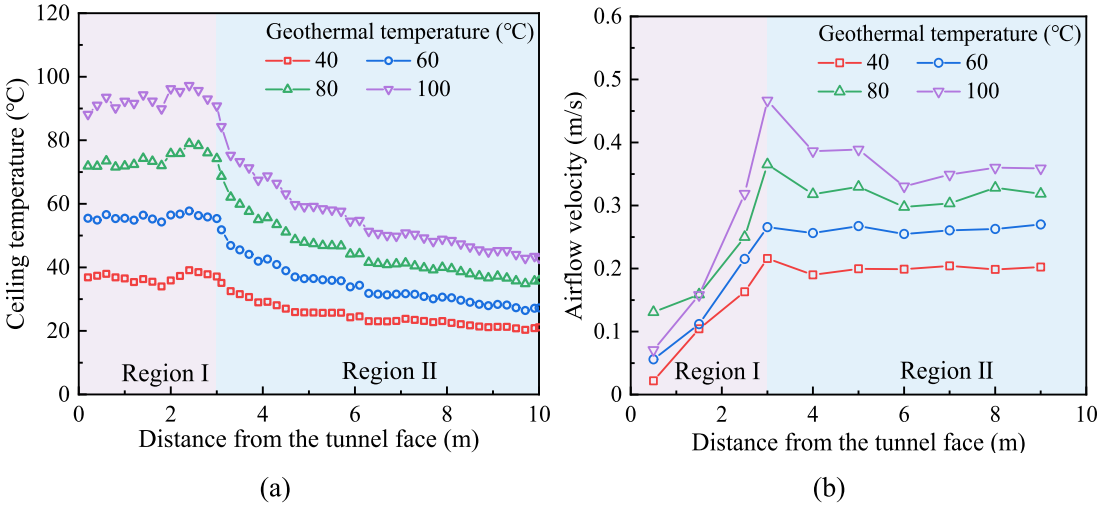

Fig. 5. Temperature and velocity distribution along the tunnel ceiling. (a) Temperature distribution, and (b) velocity distribution (Fei et al., 2025).

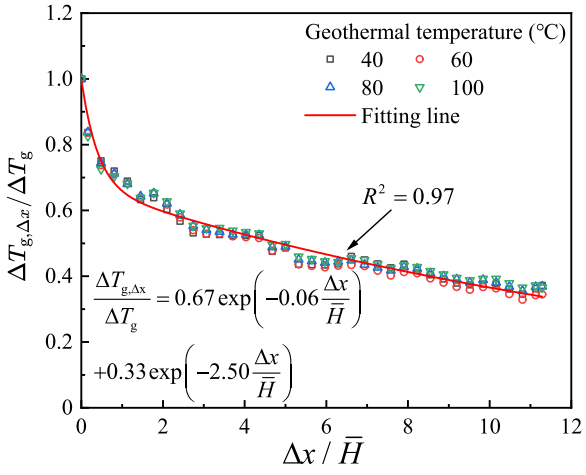

Fig. 6. Ceiling temperature distribution in the non-geothermal zone.

velocity along the tunnel ceiling remains nearly constant but still increases with the geothermal temperature. The airflow velocity distribution along the tunnel ceiling can be expressed as follows:

$$V_g^* = \frac{V_g}{\sqrt{g\bar{H}}} \sim \begin{cases} \mu\frac{x}{\bar{H}}, & \text{region I} \\ f\left(T_g^*\right), & \text{region II} \end{cases}. \tag{8}$$

Here, the coefficient μ has a good linear relationship with $\left(T_g^*\right)^3$ in the geothermal zone, and V_g^* is proportional to $\left(T_g^*\right)^3$ in the non-geothermal zone, as shown in Fig. 7. Therefore, the airflow velocity induced by geothermal conditions in the construction tunnel can be expressed using Eq. (9).

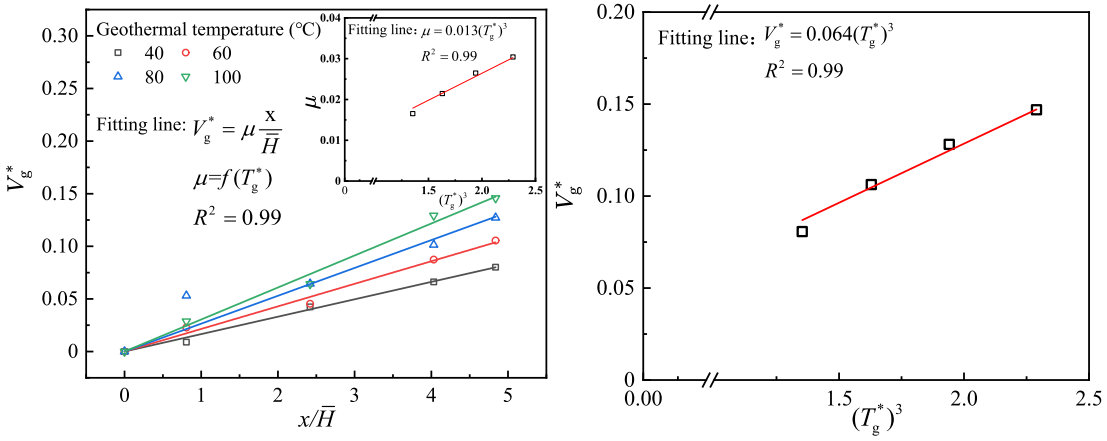

Fig. 7. (a) Relationship between V_g^* and $x/\bar{H}$, and (b) relationship between V_g^* and $\left(T_g^*\right)^3$.

$$V_g^* = \frac{V_g}{\sqrt{g\bar{H}}} = \begin{cases} 0.013\left(T_g^*\right)^3 \frac{x}{\bar{H}}, & \text{region I} \\ 0.064\left(T_g^*\right)^3, & \text{region II} \end{cases} \quad (9)$$

3.2 Smoke movement behavior

In this study, the side closer to the tunnel face is defined as upstream of the fire source, while the opposite side is defined as downstream. The upper airflow induced by geothermal conditions hinders the diffusion of the upstream smoke. The inertia of the airflow causes the upstream smoke to stagnate at a certain point. The distance between the stagnation point and the fire source is known as the smoke diffusion length, as shown in Fig. 8. Additionally, the lower airflow induced by geothermal conditions tilts the fire flame towards the tunnel face. The layered flows complicate thermal stratification in construction tunnel fires under geothermal conditions.

Several incense sticks were fixed to the tunnel ceiling and simultaneously ignited to trace smoke from the burning fuel. The sheet laser, a method that has been extensively validated in previous studies (Fan et al., 2023b; Yang et al., 2024; Zhao et al., 2024), was used to visualize the smoke. The generated smoke moves both upstream and downstream, driven by thermal buoyancy from the fire. A complex multi-layer smoke structure upstream of the fire source is observed, as shown in Fig. 9(a). A four-layer structure is observed within the range of smoke diffusion, while a three-layer structure is present outside this range. This phenomenon can be attributed to the fact that the upper hot airflow moves in the opposite direction to the upstream smoke, stopping its forward movement. Subsequently, the hot airflow descends and moves toward the fire source, entraining some smoke during this process. In the lower space of the tunnel, some smoke has a lower density than the hot airflow layer due to heat exchange. As a result, a four-layer structure of smoke-hot air-smoke-cold air is formed, while a three-layer structure of hot air-smoke-cold air is present outside the smoke diffusion range. Besides, when the smoke reaches the tunnel face, its stratification state is highly consistent with previous studies (Tong et al., 2023; L. Xu et al., 2023). Specifically, after reaching the tunnel face, the smoke flows back towards the fire source under its own buoyancy, forming a three-layer structure consisting of smoke, recirculating smoke, and air. For the downstream of the fire source, the thermal stratification is simpler, as shown in Fig. 9(b), presenting a two-layer structure of smoke and air. The upper smoke layer moves toward the open end, while cold air is supplemented from the ambient environment.

3.3 Smoke diffusion length under the tunnel ceiling

To investigate how the upstream smoke diffusion length varies with HRR and geothermal temperature, the smoke stagnation point is identified by the location of the temperature inflection point, where the smoke temperature ini-

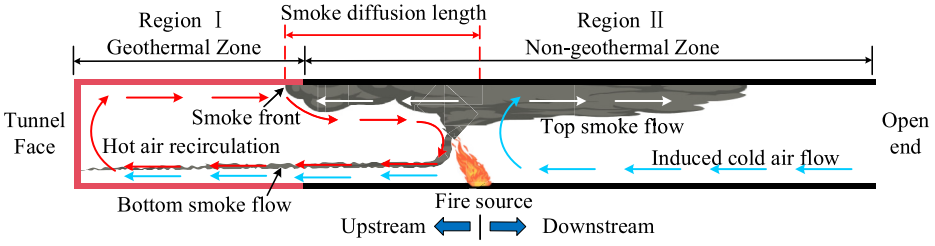

Fig. 8. Schematic of smoke movement in construction tunnels under geothermal conditions.

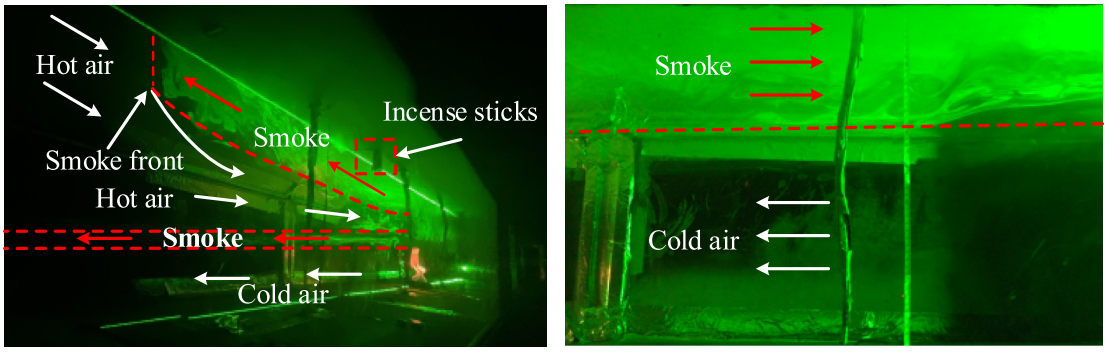

(a) (b)

Fig. 9. Thermal structure of (a) upstream and (b) downstream of the fire source.

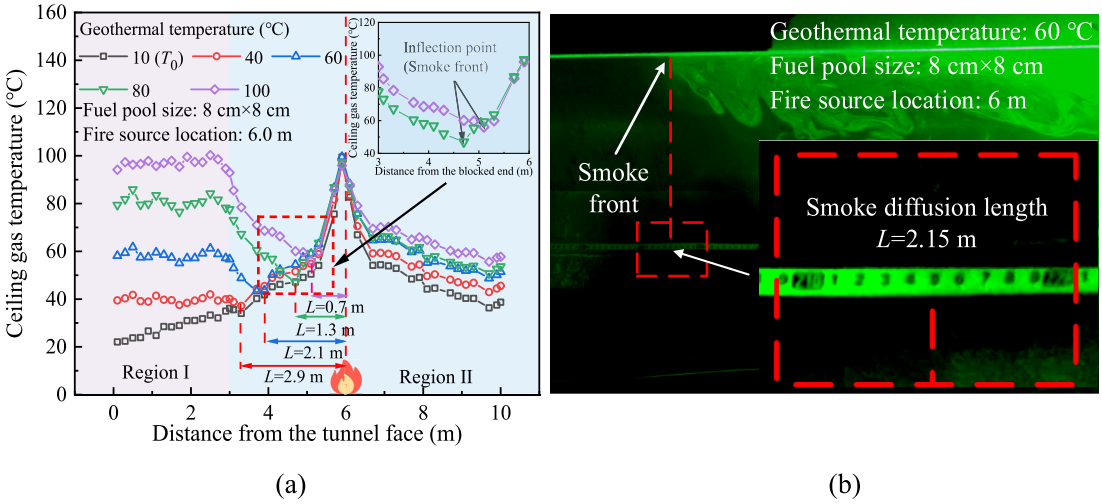

Fig. 10. Judgment of the upstream smoke diffusion length. (a) Smoke diffusion length judged by temperature, and (b) smoke diffusion length judged by laser.

tially drops and then rises again, as shown in Fig. 10(a). In most cases, the temperature inflection point does not exceed 5 K compared to baseline conditions (i.e., in the absence of fire), which is consistent with previous criteria for identifying smoke fronts (Shen et al., 2021; Fan et al., 2025). In some cases, the temperature rise may slightly exceed 5 K, potentially due to the diffusion of upstream smoke blocking hot airflow and causing hot air recirculation near the tunnel face.

To verify the reliability of the proposed judgement method, a ruler was placed on the inner wall of the tunnel to measure the smoke diffusion length, as shown in Fig. 10 (b). For a 6 m fire source located away from the tunnel face, with an 8 cm pool side length and a geothermal temperature of 60 °C, the distance calculated using the temperature inflection point criterion was 2.1 m. In comparison, the measured value was 2.15 m with the assistance of a sheet laser. The small error between the two results demonstrates the reliability of the judgement method based on the temperature inflection point.

Table 3 lists the information about the upstream smoke diffusion length under various conditions. It can be found that when the fire source is located in the geothermal zone, the smoke beneath the tunnel ceiling always reaches the tunnel face, making it impossible to measure the smoke diffusion distance. For the same fire size and fire source location, the smoke diffusion length decreases as the geothermal temperature increases. This is because the induced ceiling airflow velocity is higher under higher geothermal temperatures, increasing resistance to upstream smoke diffusion. Additionally, the higher geothermal temperature results in an elevated temperature of the induced airflow, reducing the temperature difference between the smoke and the tunnel environment, thereby decreasing

Table 3
Upstream smoke diffusion length under various conditions.

Fuel pool size	Geothermal temperature (°C)	Fire source location (m)						
		0.5	1.5	2.5	4	6	8	10
8 cm × 8 cm	10 (T_0)	–	–	–	–	–	–	–
	40	–	–	–	2.9	2.7	3.7	4.4
	60	–	–	–	1.4	2.1	2.3	3.1
	80	–	–	–	1.0	1.5	1.7	2.3
	100	–	–	–	0.7	0.9	1.3	1.7
10 cm × 10 cm	10 (T_0)	–	–	–	–	–	–	–
	40	–	–	–	–	–	4.5	5.9
	60	–	–	–	2.2	2.7	3.7	4.9
	80	–	–	–	1.4	2.1	2.7	3.5
	100	–	–	–	0.9	1.7	1.9	2.7
12 cm × 12 cm	10 (T_0)	–	–	–	–	–	–	–
	40	–	–	–	–	–	–	6.7
	60	–	–	–	–	4.0	4.5	5.9
	80	–	–	–	2.4	2.9	3.5	4.7
	100	–	–	–	2.0	2.3	2.7	3.9

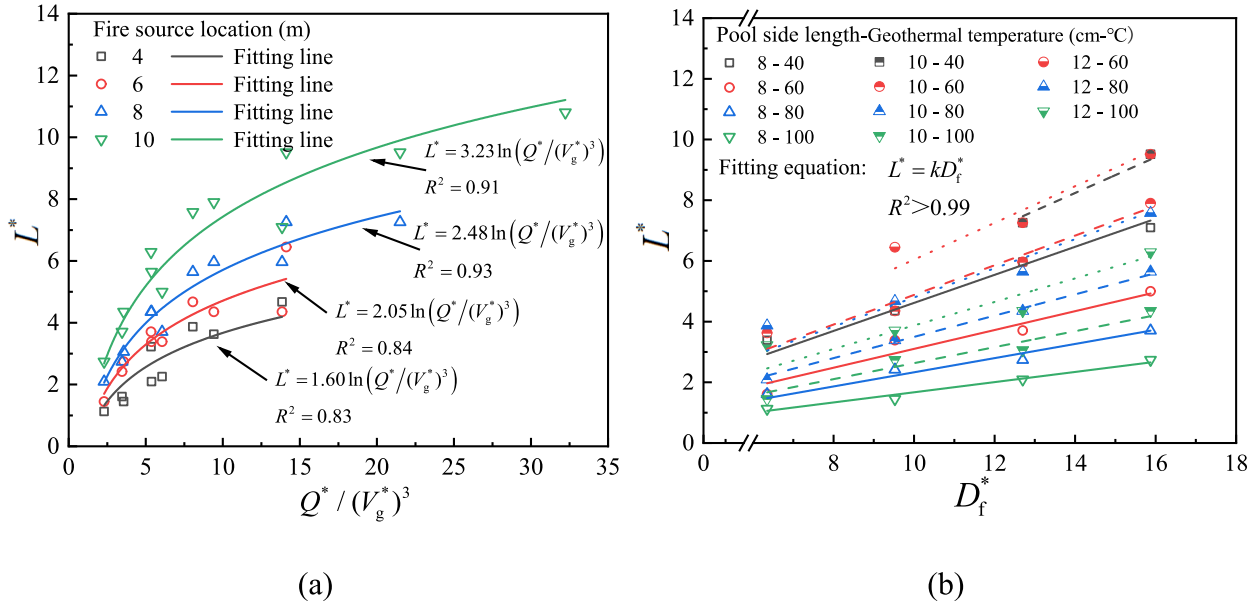

Fig. 11. Relationship between (a) L^* and $Q^*/\left(V_g^*\right)^3$, and (b) L^* and D_f^*.

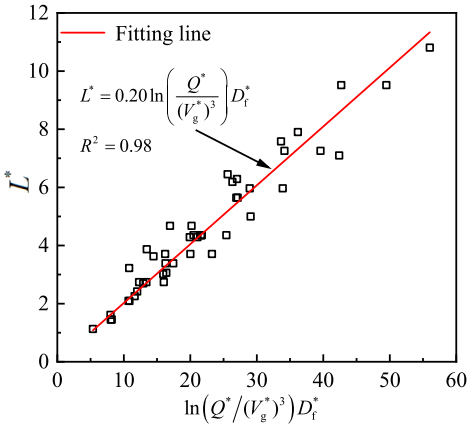

Fig. 12. Relationship between L^* and $\ln\left(Q^*/\left(V_g^*\right)^3\right)D_f^*$.

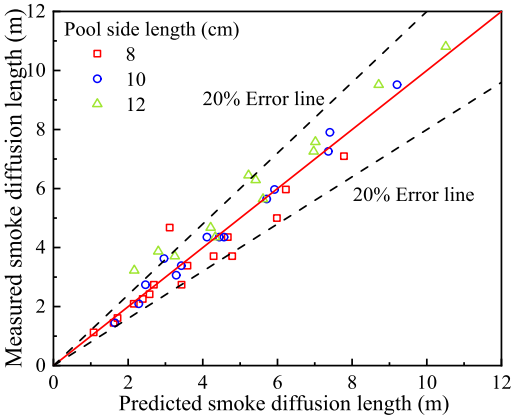

Fig. 13. Comparison between the measured and predicted smoke diffusion lengths.

the driving force for smoke diffusion. In cases with the same geothermal temperature and fire size, a fire closer to the tunnel face leads to a shorter diffusion length due to the increased tunnel environment temperature near the tunnel face. Moreover, larger fire sizes correspond to greater smoke diffusion lengths for a given geothermal temperature and fire source location.

The smoke diffusion length is related to the fire power Q, fire source location D_f, geothermal temperature T_g, air density ρ_0, the specific heat capacity of air c_p, ambient temperature T_0, gravity g, and the hydraulic height of the tunnel $\bar{H}$. The impact of T_g on the smoke diffusion length can be characterized by the induced airflow velocity V_g and the temperature in the tunnel, and the latter depends on the fire source location and ambient temperature. Therefore, we have the following function:

$$f(L) \sim f\left(Q, D_f, T_g, \bar{H}, \rho_0, c_p, T_0, g\right) \sim f\left(Q, D_f, V_g, \bar{H}, \rho_0, c_p, T_0, g\right). \quad (10)$$

By dimensional analysis, Eq. (10) can be rewritten as

$$\frac{L}{\bar{H}} \sim f\left(\frac{Q}{\rho_0 \bar{H}^2 V_g^3}, \frac{c_p T_0}{V_g^2}, \frac{g\bar{H}}{V_g^2}, \frac{D_f}{\bar{H}}\right). \quad (11)$$

Further, Eq. (11) can be simplified as follows:

$$L^* = \frac{L}{\bar{H}} \sim f\left(\frac{Q}{\rho_0 c_p T_0 g^{1/2} \bar{H}^{5/2}}\left(\frac{V_g}{\sqrt{g\bar{H}}}\right)^{-3}, \frac{D_f}{\bar{H}}\right) \sim f\left(\frac{Q^{*3}}{\left(V_g^*\right)^3}, D_f^*\right), \quad (12)$$

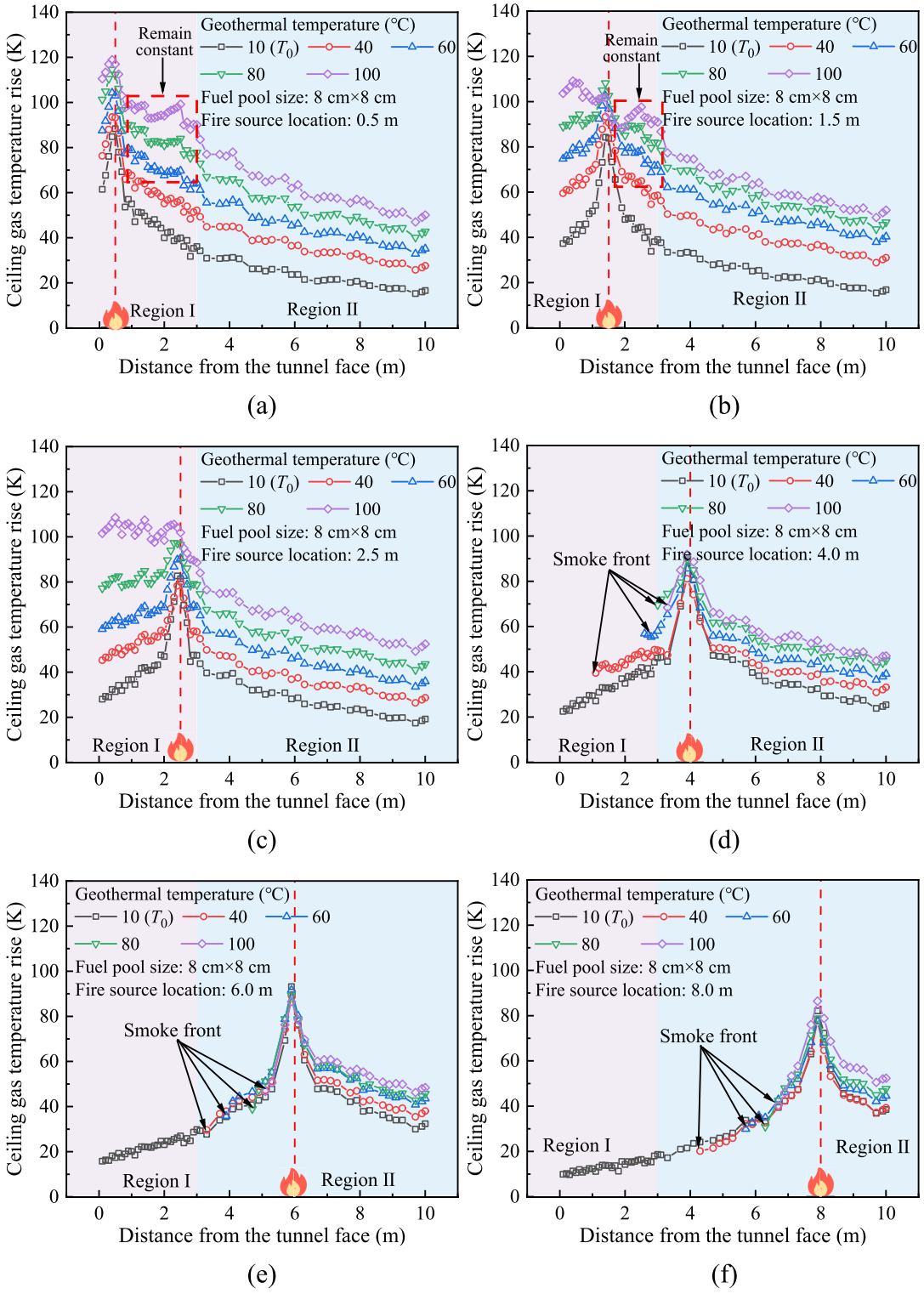

Fig. 14. Ceiling temperature distribution under varying geothermal temperatures and fire locations. (a) $D_f = 0.5$ m, (b) $D_f = 1.5$ m, (c) $D_f = 2.5$ m, (d) $D_f = 4$ m, (e) $D_f = 6$ m, (f) $D_f = 8$ m, and (g) $D_f = 10$ m.

where

$$Q^* = \frac{Q}{\rho_0 c_p T_0 g^{1/2} \bar{H}^{5/2}},\quad V_g^* = \frac{V_g}{\sqrt{g\bar{H}}},\quad D_f^* = \frac{D_f}{\bar{H}}.$$

Figure 11(a) and (b) shows the relationships between L^* and $Q^*/\left(V_g^*\right)^3$, and L^* and D_f^*, respectively. It can be observed that the logarithmic function describes the

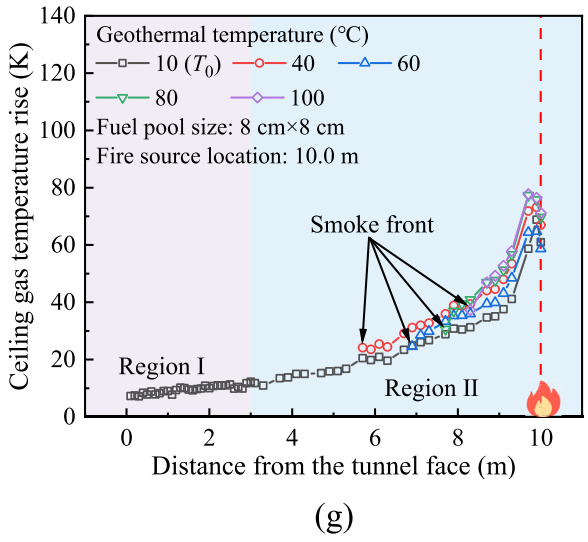

(g)

Fig 14. *(continued)*

relationship between L^* and $Q^*/\left(V_g^*\right)^3$ well, while the linear function passing through the origin effectively describes the relationship between L^* and D_f^*. Therefore, Eq. (13) can be obtained:

$$L^* = \varphi \ln\left(\frac{Q^*}{\left(V_g^*\right)^3}\right) D_f^*. \tag{13}$$

Figure 12 shows the relationships between L^* and $\ln\left(Q^*/\left(V_g^*\right)^3\right)D_f^*$. Consequently, the dimensionless smoke diffusion length can be well predicted by Eq. (14):

$$L^* = 0.20 \ln\left(\frac{Q^*}{\left(V_g^*\right)^3}\right) D_f^*. \tag{14}$$

Combined with Eq. (9), the model for predicting the smoke diffusion length can be developed as follows:

$$L^* = 0.60 \ln\left(15.6\frac{Q^{*1/3}}{\left(T_g^*\right)^3}\right) D_f^*. \tag{15}$$

Figure 13 shows a comparison between the measured and predicted smoke diffusion lengths. Results indicate that Eq. (15) can effectively predict the smoke diffusion length in construction tunnel fires under high geothermal conditions.

3.4 Ceiling temperature distribution

The decay in ceiling temperature is primarily attributed to the heat transfer between the hot smoke and the tunnel ceiling, as well as to the entrainment of lower-layer air (Lee & Ryou, 2006; Li & Ingason, 2012). Figure 14 shows the typical ceiling temperature distribution under varying geothermal temperatures and fire source locations for a pool with an 8 cm side length. It can be observed that the ceiling temperature distributions, both upstream and downstream of the fire source in construction tunnel fires under geothermal conditions, follow an exponential decay pattern, although they are asymmetrical. It is worth noting that the temperature difference is characterized by the change between the post-fire tunnel ceiling temperature and the ambient temperature, making it more convenient for assessing ceiling damage and serving as a reference for fire alarm, sprinkler, and ventilation systems.

The upstream temperature decay can be segmented into two distinct zones: the geothermal-affected zone and the non-affected zone, with the boundary at approximately 4 m, corresponding to a dimensionless fire position of 6.45 (defined as the ratio of the distance from the fire source to the tunnel face to the hydraulic diameter of the tunnel). It is important to note that the geothermal-affected zone is not identical to the heating range in the experimental design but extends slightly further. This occurs because airflow near the geothermal zone remains at elevated temperatures, and smoke temperature attenuation continues to be significantly influenced by the hot air. In the non-affected zone, as the geothermal temperature increases, the heat loss during smoke diffusion significantly decreases due to reduced convective and radiative heat transfer. Notably, when the fire source is located within the geothermal zone and at a higher temperature, the ceiling temperature in the geothermal zone remains nearly constant. This occurs because there is almost no temperature difference between the hot smoke and the surrounding environment, and the heat loss during smoke diffusion is primarily due to air entrainment, which is not reflected in the data, as the temperature measurement points are positioned near the tunnel ceiling.

The maximum ceiling temperature rise was selected as a reference point. Figure 15 shows the ceiling temperature decay downstream of the fire source, using geothermal temperatures of 40 and 100 °C as examples. Previous studies have shown that a bi-exponential model can effectively describe the ceiling temperature distribution (Ingason & Li, 2010; Gong et al., 2016). Theoretically, all curves should pass through the point (0, 1). Therefore, the following model was used to analyze the ceiling temperature distribution:

$$\frac{\Delta T_r}{\Delta T_{max}} = a\exp\left(-b\frac{r}{H}\right) + (1-a)\exp\left(-c\frac{r}{H}\right). \tag{16}$$

The temperature decay coefficients are listed in Table 4. It can be observed that fire size has a minimal effect on decay coefficients, and thus, the coefficients for different fire sizes were averaged. Furthermore, the relationship between the three decay coefficients and the dimensionless geothermal temperature is shown in Fig. 16. Finally, the ceiling temperature distribution downstream of the fire source can be well predicted by Eq. (17):

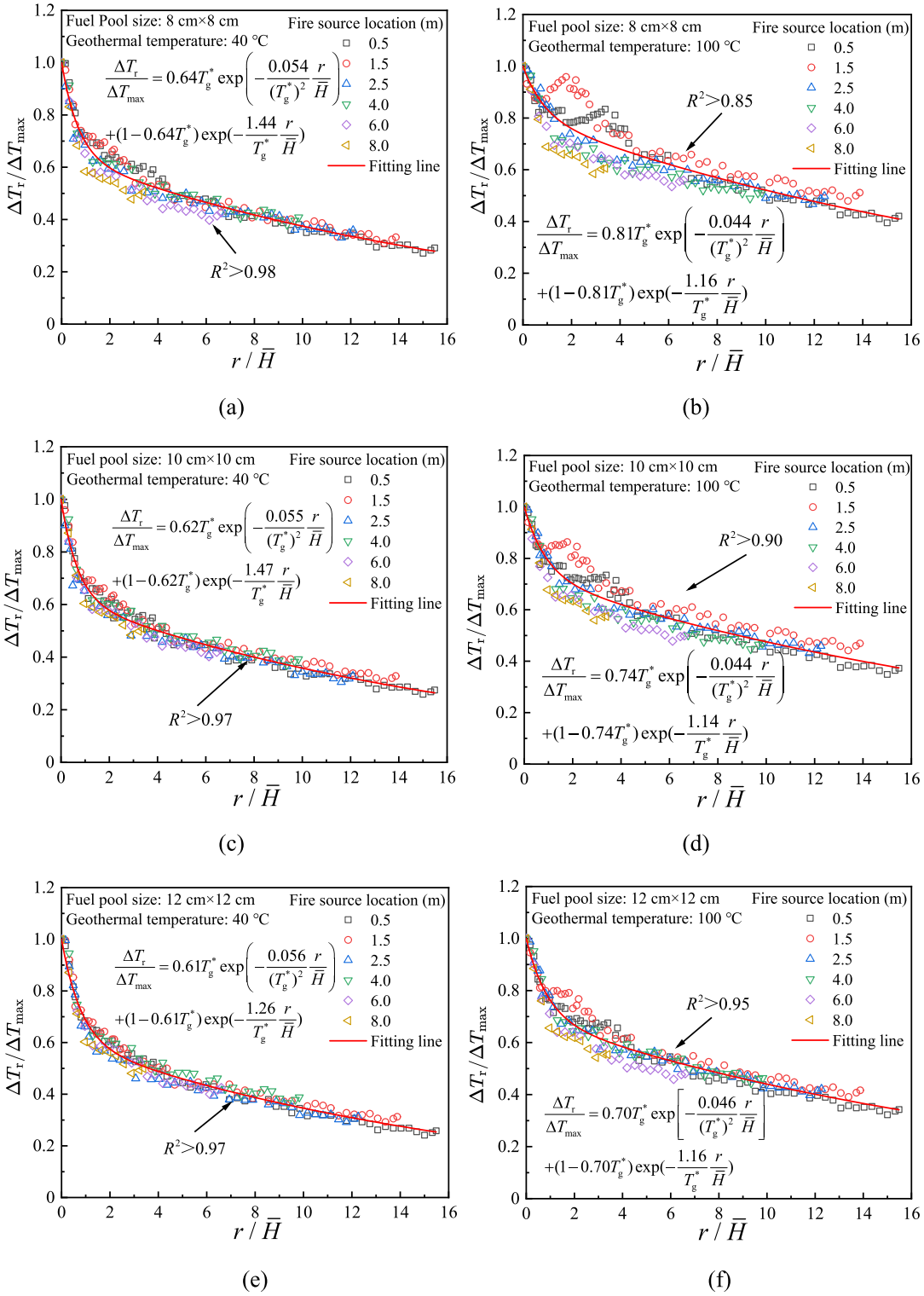

Fig. 15. Ceiling temperature decays downstream of the fire source. (a) T_g=40 °C (8 cm × 8 cm), (b) T_g=100 °C (8 cm × 8 cm), (c) T_g=40 °C (10 cm × 10 cm), (d) T_g=100 °C (10 cm × 10 cm), (e) T_g=40 °C (12 cm × 12 cm), and (f) T_g=100 °C (12 cm × 12 cm).

$$\frac{\Delta T_r}{\Delta T_{max}} = 0.57T_g^* \exp\left(-\frac{0.072}{\left(T_g^*\right)^2}\frac{r}{\overline{H}}\right) + \left(1-0.57T_g^*\right)\exp\left(-\frac{1.61}{T_g^*}\frac{r}{\overline{H}}\right). \quad (17)$$

A similar approach was applied to analyze the ceiling temperature distribution upstream of the fire source, dividing it into the geothermal-affected zone and the non-affected zone. Figure 17 shows the ceiling temperature

Table 4
Information about the downstream temperature decay coefficient.

Affected zone	Geothermal temperature (°C)	Fitting parameters			
		a	b	c	R^2
Geothermal affected zone	10 (T_0)	0.57	0.095	2.141	0.96
	40	0.70	0.088	1.906	0.94
	60	0.77	0.087	1.861	0.87
	80	0.80	0.088	1.741	0.89
	100	0.87	0.086	1.669	0.87
Non-geothermal affected zone	10 (T_0)	0.58	0.111	2.021	0.98
	40	0.65	0.108	1.619	0.94
	60	0.66	0.109	1.365	0.93
	80	0.65	0.111	1.402	0.94
	100	0.62	0.104	1.203	0.94

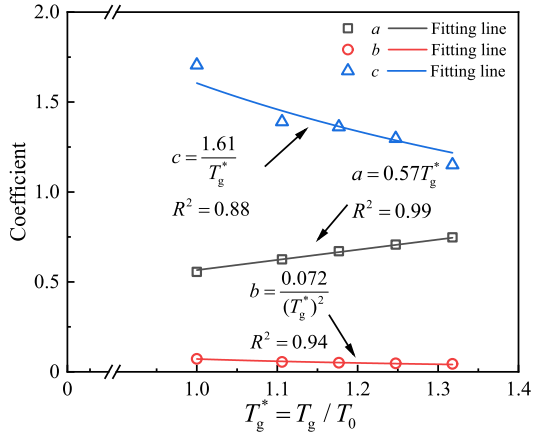

Fig. 16. Relationship between downstream temperature decay coefficients and T_g^*.

decay upstream of the fire source under various conditions. Notably, the smoke temperature remains constant because the small temperature difference between smoke and hot air in the geothermal zone was not included here. The temperature decay coefficients are presented in Table 5. It can be found that the coefficient b in the geothermal-affected zone is not sensitive to geothermal temperature, while coefficients a and b in the non-affected zone are also insensitive to geothermal temperature. Therefore, these coefficients were averaged. Similarly, the relationship between the temperature decay coefficients and the dimensionless geothermal temperature T_g^* is shown in Fig. 18. As a result, the ceiling temperature decay upstream of the fire source can be predicted by Eq. (18):

$$\frac{\Delta T_r}{\Delta T_{max}}=\begin{cases}0.43T_g^*\exp\left(-0.089\frac{r}{H}\right)+\left(1-0.43T_g^*\right)\exp\left(-\frac{2.16}{T_g^*}\frac{r}{H}\right), 0\le D_f^*\le 6.45,\\ 0.64T_g^*\exp\left(-0.11\frac{r}{H}\right)+\left(1-0.64T_g^*\right)\exp\left(-\frac{2.02}{(T_g^*)^2}\frac{r}{H}\right), 6.45<D_f^*.\end{cases} \quad (18)$$

4 Conclusions

A series of fire experiments were conducted in a 1:20 scale model tunnel to study the effects of geothermal temperature on smoke dynamics in construction tunnel fires. The flow field and temperature field induced by the geothermal condition were investigated, and the smoke diffusion and ceiling temperature distribution were analyzed. Main conclusions are as follows:

(1) In a geothermal tunnel during construction, a layered flow exists, with the upper hot airflow spreading towards the tunnel exit end and the lower cool airflow moving along the tunnel bottom. The maximum induced wind speed reaches 0.46 m/s (with a maximum geothermal temperature of 100 °C in this study). A significant correlation exists between V_g^* and $\left(T_g^*\right)^3$. Within the geothermal zone, $V_g^*=0.013\left(T_g^*\right)^3\frac{x}{H}$. Within the non-geothermal zone, $V_g^*=0.064\left(T_g^*\right)^3$. The ceiling temperature distribution remains uniform and approaches T_g in the geothermal zone, whereas in the non-geothermal zone, it follows a bi-exponential model that depends solely on T_g with a constant coefficient.

(2) The upper hot airflow hinders the diffusion of the upstream smoke, forming a multilayer smoke structure. In the geothermal zone ($D_f < 3$ m), the smoke can diffuse to the tunnel face. In the non-geothermal zone, the smoke diffusion length upstream of the fire source was analyzed. The increase in geothermal temperature significantly reduces the smoke diffusion length, e.g., when T_g

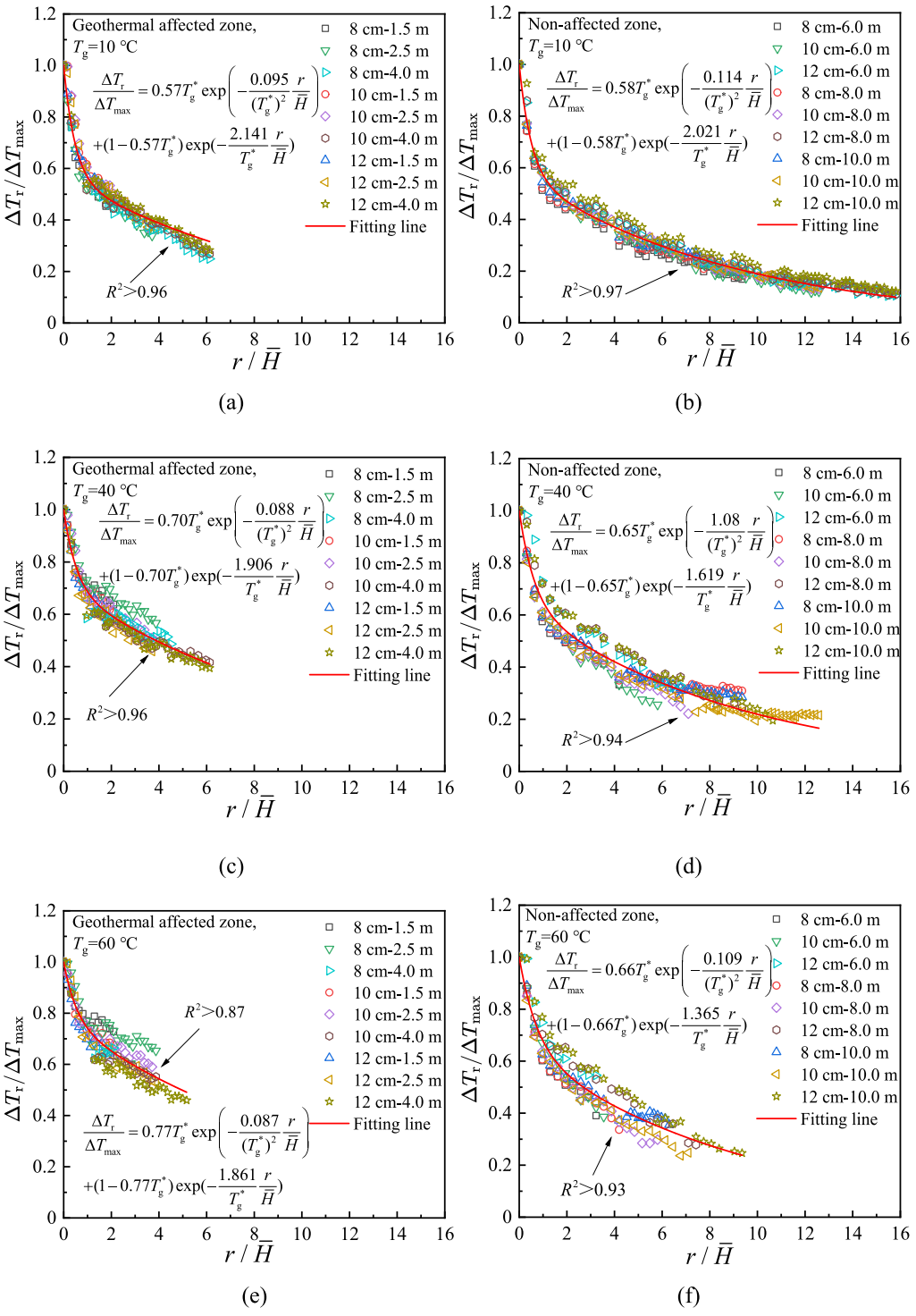

Fig. 17. Ceiling temperature decays upstream of fire source. (a) Geothermal-affected zone, T_g=10 °C , (b) non-affected zone, T_g = 10 °C , (c) geothermal-affected zone, T_g=40 °C , (d) non-affected zone, T_g=40 °C , (e) geothermal-affected zone, T_g=60 °C , (f) non-affected zone, T_g=60 °C , (g) geothermal-affected zone, T_g=80 °C , (h) non-affected zone, T_g=80 °C , (i) geothermal-affected zone, T_g=100 °C , and (j) non-affected zone, T_g=100 °C.

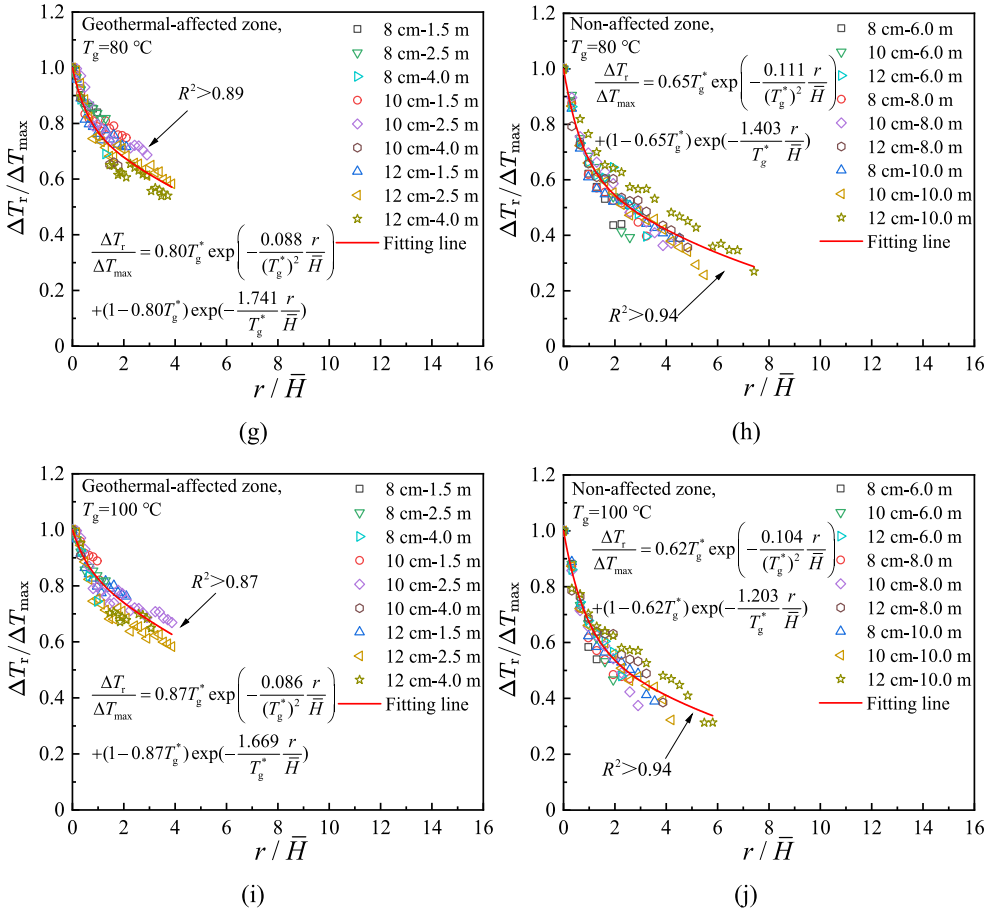

Fig 17. *(continued)*

Table 5
Information about the upstream temperature decay coefficient.

Affected zone	Geothermal temperature (°C)	Fitting parameters			
		a	*b*	*c*	R^2
Geothermal affected zone	10 (T_0)	0.57	0.095	2.141	0.96
	40	0.70	0.088	1.906	0.94
	60	0.77	0.087	1.861	0.87
	80	0.80	0.088	1.741	0.89
	100	0.87	0.086	1.669	0.87
Non-geothermal affected zone	10 (T_0)	0.58	0.111	2.021	0.98
	40	0.65	0.108	1.619	0.94
	60	0.66	0.109	1.365	0.93
	80	0.65	0.111	1.402	0.94
	100	0.62	0.104	1.203	0.94

increases from 40 to 100 °C , the smoke diffusion length decreases by 42%–76%. There is a clear linear relationship between L^* and $\ln\left(15.6\frac{Q^{*1/3}}{(T_g^*)^3}\right)D_f^*$.

(3) Ceiling temperature distribution of upstream and downstream both follow a bi-exponential model but exhibit asymmetry. The decay coefficients are related to $\left(T_g^*\right)^3$. Downstream temperature decay is insensitive to the fire location, while upstream temperature decay is divided into the geothermal-affected zone and the non-affected zone according to the fire source location. Predictive models of the upstream and downstream ceiling temperature decay along the tunnel were proposed, respectively.

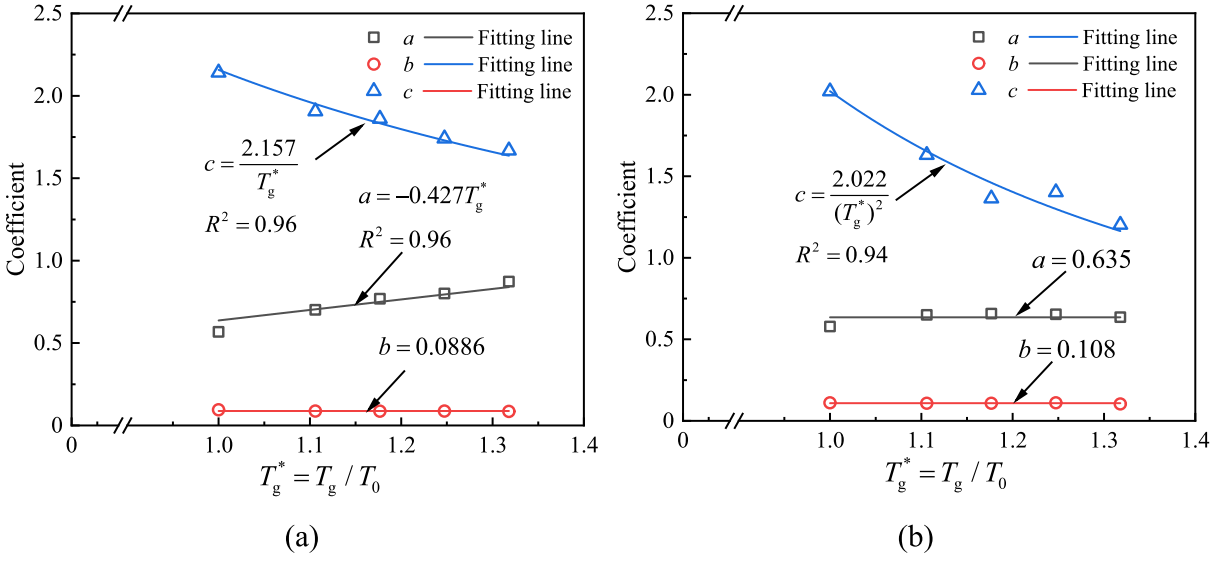

Fig. 18. Relationship between upstream temperature decay coefficients and T_g^*. (a) Geothermal affected zone, and (b) non-affected zone.

Data availability

The data that support the findings of this study are available from the corresponding author upon reasonable request.

CRediT authorship contribution statement

Chuangang Fan: Supervision, Resources, Project administration, Funding acquisition. **Xiaoxian Fei:** Writing – original draft, Methodology, Investigation, Formal analysis, Conceptualization. **Maozhen Liu:** Validation, Funding acquisition, Conceptualization. **Jiayi Ha:** Validation, Formal analysis. **Linbo Du:** Investigation, Data curation. **Zhi Li:** Writing – review & editing. **Yuhao Li:** Writing – review & editing. **Dia Luan:** Writing – review & editing.

Declaration of competing interest

The authors declare that they have no known competing financial interests or personal relationships that could have appeared to influence the work reported in this paper.

Acknowledgement

This work was supported by the National Natural Science Foundation of China (Grant No. 52278545), Natural Science Foundation of Hunan Province of China (Grant No. 2024JJ2075), the Hunan Traffic Science and Technology Project (Grant No. 202510), and the Fundamental Research Funds for the Central South University (Grant No. 2023ZZTS0416). The authors are grateful for resources from the High Performance Computing Center of Central South University.

References

Armaghani, D., Koopialipoor, M., Marto, A., & Yagiz, S. (2019). Application of several optimization techniques for estimating TBM advance rate in granitic rocks. *Journal of Rock Mechanics and Geotechnical Engineering, 11*(4), 779–789.

Chaabat, F., Creyssels, M., Mos, A., Wingrave, J., Correia, H., Marro, M., & Salizzoni, P. (2019). The effects of solid barriers and blocks on the propagation of smoke within longitudinally ventilated tunnels. *Building and Environment, 160*, 106207.

Chen, L., Yang, S., Guo, L., Zhang, P., Li, K., Shao, W., Xu, X., & Sun, F. (2023a). Seismic ahead-prospecting based on deep learning of retrieving seismic wavefield. *Underground Space, 11*, 262–274.

Chen, X., Zhou, X., Zhong, Z., Liang, N., Wang, Y., & Zhang, X. (2023b). Study on temperature field and influencing factors of the high geothermal tunnel with extra-long one-end construction ventilation. *International Journal of Thermal Sciences, 191*, 108322.

Fan, C., Luan, D., Bu, R., Sheng, Z., Wang, F., & Huang, X. (2023a). Can heavy rainfall affect the burning and smoke spreading characteristics of fire in tunnels?. *International Journal of Heat and Mass Transfer, 207*, 123972.

Fan, C., Zeng, W., Jiao, A., Chen, H., Bu, R., An, W., & Ni, S. (2023b). Study of critical velocity and back-layering length with fire sources both inside and outside a tunnel. *Fire Safety Journal, 141*, 103931.

Fan, C., Liu, M., Fei, X., Ha, J., Du, L., Jiao, A., & Li, Y. (2025). Experimental study on smoke movement characteristics and temperature distribution in high geothermal tunnel fire during construction with shaft structures. *Tunnelling and Underground Space Technology, 159*, 106470.

Fei, X., Liu, M., Ha, J., Du, L., Li, Z., Li, Y., & Fan, C. (2025). Experimental study on burning rate and flame geometry in construction tunnel fires under high geothermal conditions. *Deep Underground Science and Engineering*, 1–13.

Gao, Z., Li, L., Zhong, W., & Liu, X. (2021). Characterization and prediction of ceiling temperature propagation of thermal plume in confined environment of common services tunnel. *Tunnelling and Underground Space Technology, 110*, 103714.

Gao, Z., Zhao, P., Fan, Y., & Chen, Y. (2024). Influence of the closed end on the smoke propagation and temperature profile in urban utility tunnel fires. *Tunnelling and Underground Space Technology, 150*, 105852.

Gong, L., Jiang, L., Li, S., Shen, N., Zhang, Y., & Sun, J. (2016). Theoretical and experimental study on longitudinal smoke temperature distribution in tunnel fires. *International Journal of Thermal Sciences, 102*, 319–328.

Guo, Y., Yuan, Z., Yuan, Y., Cao, X., & Zhao, P. (2021). Numerical simulation of smoke stratification in tunnel fires under longitudinal velocities. *Underground Space, 6*(2), 163–172.

Han, J., Geng, P., Wang, Z., Lu, Y., Wang, F., Wen, J., & Liu, F. (2022). Effect of ceiling extraction on the smoke spreading characteristics and temperature profiles in a tunnel with one closed end. *Tunnelling and Underground Space Technology, 119*, 104236.

Hu, Y., Wang, M., Wang, Q., Liu, D., & Tong, J. (2019). Field test of thermal environment and thermal adaptation of workers in high geothermal tunnel. *Building and Environment, 160*, 106174.

Hu, Y., Wang, Q., Wang, M., & Liu, D. (2021). A study on the thermo-mechanical properties of shotcrete structure in a tunnel, excavated in granite at nearly 90 °C temperature. *Tunnelling and Underground Space Technology, 110*, 103830.

Ingason, H., & Li, Y. (2010). Model scale tunnel fire tests with longitudinal ventilation. *Fire Safety Journal, 45*(6), 371–384.

Lee, S., & Ryou, H. (2006). A numerical study on smoke movement in longitudinal ventilation tunnel fires for different aspect ratio. *Building and Environment, 41*(6), 719–725.

Li, L., Zhang, W., Gao, Z., Yang, L., Du, F., Wang, L., Wei, L., & Huang, F. (2023). Experimental study on the maximum temperature under the ceiling in a metro depot with one end closed. *Tunnelling and Underground Space Technology, 134*, 104968.

Li, Y., & Ingason, H. (2012). The maximum ceiling gas temperature in a large tunnel fire. *Fire Safety Journal, 48*, 38–48.

Liu, C., Cheng, H., Nie, W., Jiang, S., Chen, J., Lin, P., & Zhong, M. (2023). Study on smoke propagation in tunnel construction of a hydropower station: A full-scale fire experiment. *Journal of Safety Science and Resilience, 4*(2), 188–202.

Liu, R., Jiang, D., He, Y., Zhang, H., Chen, J., Ren, S., & Zhou, Z. (2024). Study on cooling measures and ventilation cooling device of high ground temperature tunnel. *Journal of Thermal Analysis and Calorimetry, 149*(8), 3347–3365.

Liu, M., Fei, X., Luan, D., Tong, Y., Jiao, A., Ha, J., Li, Y., & Fan, C. (2025). Smoke control using natural ventilation shafts in a tunnel during construction under the effect of geothermal condition. *Fire Safety Journal, 152*, 104340.

Luan, D., Bielawski, J., Bu, R., Węgrzyński, W., Fan, C., & Huang, X. (2025). Fire and smoke transport dynamics in a dead-end tunnel under heavy rainfall. *International Journal of Heat and Mass Transfer, 236*, 126270.

Ouyang, R., Zhao, W., Yang, L., Jiao, A., Xu, Z., & Fan, C. (2021). An experimental investigation of burning rate and flame geometric parameters of tunnel fires under canyon cross wind and longitudinal ventilation. *Fire Safety Journal, 126*, 103474.

Shen, Y., Jiao, A., Chen, T., Li, Y., Gao, Y., Xu, Z., Jiang, B., & Fan, C. (2021). Experimental study on smoke movement characteristics in tunnel fires with different canyon cross wind yaw angles. *Tunnelling and Underground Space Technology, 117*, 104129.

Tang, Z., Gao, K., Tao, C., Liu, Y., & Qi, Z. (2024). The influence of tunnel aspect ratio on the gas temperature distribution in advancing tunnel. *Tunnelling and Underground Space Technology, 149*, 105818.

Tao, F., & Bobet, A. (2016). Effect of temperature on deep lined circular tunnels in transversely anisotropic elastic rock. *Underground Space, 1*(2), 79–93.

Tong, W., Ge, F., Ding, L., Ji, J., Zhou, Y., Zhou, Y., & Zhou, F. (2023). Full-scale experimental and numerical study of smoke spread characteristics in a long-closed channel with one lateral opening. *Tunnelling and Underground Space Technology, 132*, 104919.

Wan, H., Jiang, Y., & Jiang, J. (2023). A survey of fire accidents during the process of highway tunnel operation in China from 2010 to 2021: Characteristics and countermeasures. *Tunnelling and Underground Space Technology, 139*, 105237.

Wang, M., Hu, Y., Liu, D., Jiang, C., Wang, Q., & Wang, Y. (2020). A study on the heat transfer of surrounding rock-supporting structures in high-geothermal tunnels. *Applied Sciences, 10*(7), 2307.

Wang, Y., Zhou, X., Liu, X., Chen, X., Xu, Q., & Wang, Q. (2023). Ambient temperature prediction model and cooling requirement analyze in the high-altitude construction tunnel passing through the abnormally high geothermal region. *Tunnelling and Underground Space Technology, 141*, 105360.

Xu, D., Zhang, B., Ai, Z., Bu, X., Pan, H., & Chen, S. (2023a). Spatial-temporal evolution principle of temperature field in a high-temperature geothermal highway tunnel. *Ain Shams Engineering Journal, 14*(5), 101965.

Xu, G., Zhu, G., Pan, R., & Liu, X. (2021a). Investigation on temperature distribution under the coupling action of transverse position and fire sealing of linear fire in tunnel. *Case Studies in Thermal Engineering, 26*, 101032.

Xu, L., Qiu, M., Zhao, Y., Ding, C., Yu, W., Zhao, S., Li, L., & Liu, J. (2023b). Experimental study on vertical temperature distribution of the two-layer smoke flow in tunnel during construction. *Tunnelling and Underground Space Technology, 136*, 105105.

Xu, Y., Li, Z., Wang, J., Chen, Y., Li, R., Wang, Q., & Jia, M. (2022). Ventilation and heat exchange characteristics in high geotemperature tunnels considering buoyancy-driven flow and groundwater flow. *International Journal of Thermal Sciences, 173*, 107400.

Xu, Z., Wang, W., Lin, P., Nie, L., Wu, J., & Li, Z. (2021b). Hard-rock TBM jamming subject to adverse geological conditions: Influencing factor, hazard mode and a case study of Gaoligongshan Tunnel. *Tunnelling and Underground Space Technology, 108*, 103683.

Yang, D., Guo, X., Jiang, L., & Du, T. (2024). Prediction model of buoyancy-driven flow rate in inclined tunnels with a localized buoyancy source: Emphasis on stratification effects. *Building and Environment, 250*, 111165.

Yang, D., Jiang, S., Huang, F., Hu, Z., & Liu, X. (2023). Characteristics of hot airflow in high-temperature tunnels under natural ventilation. *Journal of Railway Science and Engineering, 20*(4), 1433–1444.

Yao, Y., Cheng, X., Zhang, S., Zhu, K., Zhang, H., & Shi, L. (2017). Maximum smoke temperature beneath the ceiling in an enclosed channel with different fire locations. *Applied Thermal Engineering, 111*, 30–38.

Ye, K., Tang, X., Zheng, Y., Ju, X., Peng, Y., Liu, H., Wang, D., Cao, B., & Yang, L. (2021). Estimating the two-dimensional thermal environment generated by strong fire plumes in an urban utility tunnel. *Process Safety and Environmental Protection, 148*, 737–750.

Ye, K., Zhou, X., Zheng, Y., Liu, H., Tang, X., Cao, B., Huang, Y., Chen, Y., & Yang, L. (2019). Estimating the longitudinal maximum gas temperature attenuation of ceiling jet flows generated by strong fire plumes in an urban utility tunnel. *International Journal of Thermal Sciences, 142*, 434–448.

Yu, P. Y. (2015). Research on the high ground temperature risk during long tunnel construction. In *Proceedings of the International Conference on Advances in Energy, Environment and Chemical Engineering*, Changsha, China.

Zhang, D., Sun, Z., & Fang, Q. (2022). Scientific problems and research proposals for Sichuan–Tibet railway tunnel construction. *Underground Space, 7*(3), 419–439.

Zhang, J., Li, W., Tang, X., Tian, J., Wang, Y., Guo, Q., & Pang, Z. (2017). Geothermal data analysis at the high-temperature hydrothermal area in Western Sichuan. *Science China Earth Sciences, 60*(8), 1507–1521.

Zhao, J., Wang, Z., Hu, Z., Cui, X., Peng, X., & Zhang, J. (2023a). Effects of fire location and forced air volume on fire development for single-ended tunnel fire with forced ventilation. *Fire, 6*(3).

Zhao, K., Yuan, Y., Jiang, F., & Cao, X. (2023b). Numerical investigation on temperature–humidity field under mechanical ventilation in the construction period of hot-humid tunnel along the Sichuan–Tibet Railway. *Underground Space, 8*, 123–143.

Zhao, X., Chi, J., Luo, H., Zhou, R., Hao, M., & Jiang, J. (2024). Effect of unpowered ventilation caps and shaft parameters on fire smoke spread in the natural ventilation tunnel with shafts. *Journal of Building Engineering, 87*, 109086.

Zhao, Z., Xu, H., Liu, G., Liu, F., & Wang, G. (2021). A robust numerical method for modeling ventilation through long tunnels in high temperature regions based on 1D pipe model. *Tunnelling and Underground Space Technology, 115*, 104050.